Hauser-Feshbach fission fragment de-excitation with calculated macroscopic-microscopic mass yields

Patrick Jaffke,* Peter Möller, Patrick Talou, and Arnold J. Sierk
Theoretical Division, Los Alamos National Laboratory, Los Alamos, New Mexico 87545, USA

(Received 20 December 2017; published 15 March 2018)

The Hauser-Feshbach statistical model is applied to the de-excitation of primary fission fragments using input mass yields calculated with macroscopic-microscopic models of the potential energy surface. We test the sensitivity of the prompt fission observables to the input mass yields for two important reactions, ^{235}U$(n_{\rm th}, f)$ and ^{239}Pu$(n_{\rm th}, f)$, for which good experimental data exist. General traits of the mass yields, such as the location of the peaks and their widths, can impact both the prompt neutron and γ-ray multiplicities, as well as their spectra. Specifically, we use several mass yields to determine a linear correlation between the calculated prompt neutron multiplicity $\bar{\nu}$ and the average heavy-fragment mass $\langle A_h \rangle$ of the input mass yields $\partial\bar{\nu}/\partial\langle A_h\rangle = \pm 0.1\ (n/f)$/u. The mass peak width influences the correlation between the total kinetic energy of the fission fragments and the total number of prompt neutrons emitted, $\bar{\nu}_T$(TKE). Typical biases on prompt particle observables from using calculated mass yields instead of experimental ones are $\delta\bar{\nu} = 4\%$ for the average prompt neutron multiplicity, $\delta\overline{M}_\gamma = 1\%$ for the average prompt γ-ray multiplicity, $\delta\bar{\epsilon}_n^{\rm LAB} = 1\%$ for the average outgoing neutron energy, $\delta\bar{\epsilon}_\gamma = 1\%$ for the average γ-ray energy, and $\delta\langle{\rm TKE}\rangle = 0.4\%$ for the average total kinetic energy of the fission fragments.

DOI: 10.1103/PhysRevC.97.034608

I. INTRODUCTION

Nearly 80 years have passed since Hahn and Straßmann observed fission products following the bombardment of uranium with neutrons [1,2]. The data were explained by Meitner and Frisch as the result of a division of a nucleus into two fragments using an analogy with a liquid drop [2]. Shortly after, Bohr and Wheeler put this analogy on a quantitative footing, allowing them to calculate fission-barrier heights fairly well throughout the nuclear chart [3,4]. Since 1938, our theoretical description of fission has continually improved. For example, fission-barrier saddle-point heights are calculated within ∼1 MeV of the empirical values [5] and realistic descriptions of the fragment mass distributions across the (N, Z) plane are possible [6].

Fission begins with the formation of a compound state [7]. The subsequent process leading to the formation of separate fragments can be described as an evolution in a potential-energy landscape, where each location corresponds to a specific nuclear shape. A large number of fragment excitation energies, shapes, and mass splits result, with different formation probabilities. The fragments de-excite by neutron and γ-ray emissions. β decay and delayed-neutron emission follow as these unstable nuclei decay towards β stability. Over the years, considerable advancements have been made in studies of these different processes. For example, some fragment properties have been reasonably well reproduced using macroscopic-microscopic descriptions of the potential-energy surface based on Brownian shape-motion dynamics [8,9] or Langevin equations [10,11], or microscopic models based on effective nucleon-nucleon interactions in terms of energy-density functionals in an adiabatic approximation [12,13] or with full nonadiabatic effects included [14,15]. In addition, models of the de-excitation via sequential emission of neutrons and γ rays [16–18] have been used to describe various prompt neutron and γ-ray data. Finally, the delayed-neutron emission and half-lives via β-n decays have also been investigated based on a quasiparticle random phase approximation treatment of transitions in deformed nuclei [19]. Despite eight decades of progress in modeling some of the individual steps from scission to the formation of β-stable fragments, no complete, cohesive model tying together the various correlated quantities exists.

In this work, we combine mass yields determined from macroscopic-microscopic descriptions of the potential-energy surface for the compound nucleus shape and dynamics based on either the Brownian shape-motion [8] or Langevin approach [11] with a de-excitation model based on a Monte Carlo implementation of the Hauser-Feshbach statistical-decay theory [20]. Using theoretical models for the fission-fragment yields is attractive for many reasons. Most notably, the best-studied fission reactions are restricted to a handful of actinides at a few incident neutron energies, but recent experimental methods have been used to probe fragment yields beyond this region [21,22]. Even so, astrophysical r-process calculations would require yields for thousands of nuclei [23]. Additionally, many yields-measurement techniques rely on assumptions about the prompt neutron emission from the primary fragments [24,25]. Another issue is that the inherent mass resolution in experimental measurements will smear the true yields, and only a few detector setups have been able to achieve the difficult goal of a resolving power less than

*Corresponding author: pjaffke@lanl.gov

one nucleon [26–29]. By connecting theoretical calculations of the fragment yields with a de-excitation model, one can both estimate fission observables for unknown reactions and improve our understanding of current experimental data. We use this connection to determine correlations between the characteristics of the mass yields and the prompt neutron and γ-ray emissions. In this way, experimental measurements of prompt fission observables can inform the development of more accurate fission models and de-excitation methods. We utilize two commonly studied fission reactions, ^{235}U$(n_{\rm th},f)$ and ^{239}Pu$(n_{\rm th},f)$, as large amounts of experimental data are available on both the fragment yields and many prompt fission observables.

Section II introduces the main theoretical components of the macroscopic-microscopic model and the Hauser-Feshbach treatment. We first compare calculated and experimental mass yields. Then, we compute in Sec. III the prompt neutron and γ-ray emissions with both sets of input yields. Comparisons between the prompt observables, such as the neutron and γ-ray multiplicities and spectra, are made and we identify the causes of the observed differences. In Sec. IV, we conclude by providing estimates of the biases introduced by using calculated yields instead of experimental ones and identify future improvements and uses for these theoretical models.

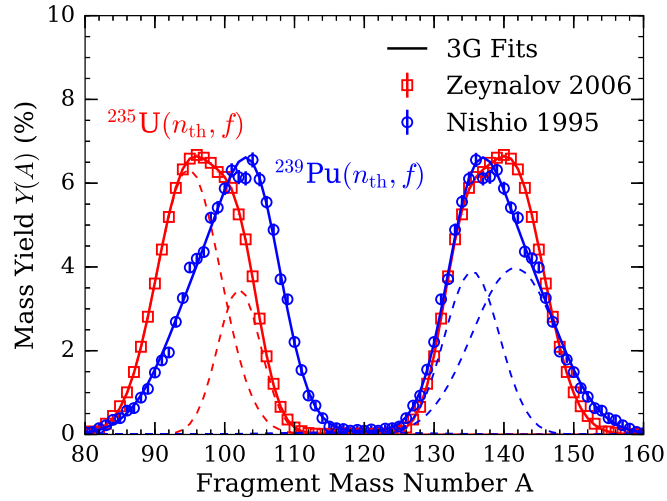

FIG. 1. The three-Gaussian parametrization [Eq. (1)] is used to fit two experimental mass yields. The squares are for ^{235}U$(n_{\rm th},f)$ from Ref. [33] and the circles are for ^{239}Pu$(n_{\rm th},f)$ from Ref. [34]. The dashed lines are the individual Gaussians and the solid curves are the full three-Gaussian fit.

II. THEORETICAL MODELS

A. Yield calculation

The complete specifications of the yield models used here are in Refs. [9,11]. The Brownian shape-motion model used here represents a generalization of the model introduced in Ref. [8]. In its original formulation, fission-fragment yields were obtained as a function of nucleon number A. Since it was assumed that the fragment charge-asymmetry ratios Z/N were both equal to the charge asymmetry of the compound fissioning system, one also obtained charge yields. After further development the model now provides the two-dimensional yield $Y(Z,N)$ versus fragment proton and neutron numbers and takes into account pairing effects in the nascent fragments. To illustrate the main features of the model we briefly outline the original implementation of Ref. [8]. The first step is to calculate the nuclear potential energy as a function of a discrete set of five shape variables, namely elongation, neck diameter, the (different) spheroidal deformations of the two nascent fragments, and the mass asymmetry of the nascent fragments. To represent with sufficient accuracy this five-dimensional potential-energy function based on a discrete set of shapes, we calculate the potential energy for more than five million different shapes. The yield is obtained by calculating random walks in this potential-energy landscape. A starting point, normally the second minimum, is selected. At any time during the walk a neighbor point to the current point is randomly selected as a candidate for the next point on the random trajectory. This becomes the next point on the trajectory if it is lower in energy than the current point; if it is higher in energy it may become the next point on the trajectory with probability $\exp(-\Delta V/T)$ where ΔV is the energy difference between the candidate point and current point. The process is repeated until a shape with neck radius smaller than a selected value for the scission radius is reached. The values of the shape parameters and potential energy at this endpoint are tabulated and a new random walk is started. In this way ensembles of various scission parameters are obtained. The method and its current extensions are discussed and benchmarked in Refs. [6,8,9,30,31]. The Langevin model starts from essentially the same macroscopic-microscopic description of the potential-energy surface as the Brownian shape-motion model, while including full dynamical inertial and dissipative effects on fission trajectories. It is currently limited to the assumption of a fixed Z/N ratio, as were the first Brownian shape-motion model calculations [8].

We parametrize the mass yields with the common three-Gaussian parametrization, similar to the Brosa modes [32], to generate the input for a Hauser-Feshbach calculation. The Gaussians are given by their mean μ_i, variance σ_i^2, and amplitude w_i as

$$G_i(A) = \frac{w_i}{\sqrt{2\pi\sigma_i^2}} \times \left[\exp\left(\frac{-(A-\mu_i)^2}{2\sigma_i^2}\right) + \exp\left(\frac{-[A-(A_0-\mu_i)]^2}{2\sigma_i^2}\right)\right], \quad (1)$$

where the indices $i = 1,2,3$ refer to the three Gaussians. The Gaussian centered around the symmetric masses $i = 3$ has a fixed mean $\mu_3 = A_0/2$, with A_0 being the mass of the fissioning nucleus. In addition, the total yields are required to sum to 2: $w_1 + w_2 + w_3 = 2$. These requirements reduce the number of variables to seven for each $Y(A)$. As seen in Fig. 1, the three-Gaussian fit is an excellent match to the experimental data for both the ^{235}U$(n_{\rm th},f)$ reaction [33] and the ^{239}Pu$(n_{\rm th},f)$ reaction [34]. We note that the three-Gaussian parametrization is a smooth fit, so it cannot include shell effects. Nevertheless, this parametrization captures the major aspects of the mass

yields, so we use it as the input mass yields in the de-excitation calculations.

B. Fragment de-excitation

The fragment de-excitation process is calculated in the statistical decay theory of Hauser and Feshbach [35]. In this formalism, the probabilities for neutron and γ-ray emission from the excited fragments are calculated at each stage of the decay. These probabilities are derived from the transmission coefficients and level densities via

$$P(\epsilon_n)d\epsilon_n \propto T_n(\epsilon_n)\rho(A-1,Z,E-\epsilon_n-S_n)d\epsilon_n,$$
$$P(\epsilon_\gamma)d\epsilon_\gamma \propto T_\gamma(\epsilon_\gamma)\rho(A,Z,E-\epsilon_\gamma)d\epsilon_\gamma, \quad (2)$$

where the neutron transmission coefficients T_n are computed using an optical model with the global optical potential of Koning and Delaroche [36]. The γ-ray transmission coefficients T_γ come from the strength functions in the Kopecky-Uhl formalism [37] for the different multipolarities considered. The values for the strength-function parameters are taken from the Reference Input Parameter Library (RIPL-3) [38]. The level densities ρ are functions of the fragment mass A, charge Z, and excitation energy E of the final nuclear state. They are calculated in the Gilbert-Cameron formalism [39], where the low excitation energy discrete states are used to create a constant temperature model that connects smoothly to the higher excitation energy continuum states in a Fermi-gas model. Here, S_n is the neutron separation energy of a fragment with Z protons and A nucleons. Thus, with Eq. (2), one can determine the probability for a given fragment with excitation energy E to emit either a neutron with energy ϵ_n or a γ ray with energy ϵ_γ. In the Monte Carlo implementation of the Hauser-Feshbach statistical theory [20], the probabilities are sampled at each step of the de-excitation until the fragments reach a long-lived isomer or their ground state. This is done for many fission events resulting in a large data set, where the energy, spin, and parity are conserved on an event-by-event basis.

To initiate the Hauser-Feshbach decay simulation, one must identify the initial pre-neutron emission fragment distribution and the excitation energy, spin, and parity distributions. The mass A, charge Z, and total kinetic energy TKE distribution $Y(A,Z,\mathrm{TKE})$ is sampled to acquire the initial fragment characteristics of a particular fission event. The total excitation energy TXE between the two complementary fragments is then

$$\mathrm{TXE} = [E_n + B_n + M(A_0,Z_0) - M(A_l,Z_l) - M(A_h,Z_h)] - \mathrm{TKE}(A_h), \quad (3)$$

where l and h denote the light and heavy fragments, respectively. The mass and charge of the fissioning nucleus are A_0 and Z_0 and, in the case of neutron-induced fission, E_n is the incident neutron energy and B_n is the binding energy of the target. Thus, the first term on the right-hand side in Eq. (3) represents the Q value of the reaction, with $M(A,Z)$ being the mass of a nucleus with mass number A and charge Z.

Next, the TXE is shared between the two fragments. There are several proposed methods of doing this [40–42] and the choice of method can dramatically affect some fission observables, particularly the average prompt neutron multiplicity as a function of the fragment mass $\bar{\nu}(A)$ [43,44]. We use the CGMF code [45], which is described in Refs. [20,46], to perform the Monte Carlo treatment of the Hauser-Feshbach decay. The TXE is shared via a ratio of nuclear temperatures R_T with

$$R_T^2 = \frac{T_l^2}{T_h^2} \approx \frac{E_l a_h}{E_h a_l}, \quad (4)$$

where the approximation assumes a Fermi-gas model for the level density to relate the energy E_i to the level-density parameter a_i and the temperature T_i. With $\mathrm{TXE} = E_l + E_h$ and rearranging Eq. (4), we have

$$E_h = \mathrm{TXE}\frac{a_h}{R_T^2 a_l + a_h}. \quad (5)$$

The level density parameters depend on the excitation energy of the corresponding fragments $a_i \equiv a_i(E_i)$, so we iteratively solve the right-hand side of Eq. (5) with a given E_l and E_h and corresponding a_l and a_h, then adjust E_l and E_h until the chosen R_T value is satisfied. In general, R_T can have a mass dependence: $R_T \equiv R_T(A)$. While adjusting $R_T(A)$ in order to reproduce the experimental $\bar{\nu}(A)$, we have found that it has little impact on our results.

One key ingredient for the simulation is the initial spin distribution of the fission fragments. As the Hauser-Feshbach model conserves angular momentum, the spin and parity are needed in order to match levels through γ-ray emission of different multipolarities. Currently, $E1$, $M1$, and $E2$ transitions are considered in CGMF. The spin J distribution follows a Gaussian form,

$$P(J) \propto (2J+1)\exp\left[\frac{-J(J+1)\hbar^2}{2\alpha T \mathcal{I}_0(A,Z)}\right], \quad (6)$$

where T is the nuclear temperature determined from the level density parameter a and the excitation energy E. The term $\mathcal{I}_0(A,Z)$ is the moment of inertia for a rigid rotor of the ground-state shape of a fragment with a particular mass and charge. The factor α is a spin-scaling factor, which can be used to adjust the average spin of the fragments [47]. Previous studies have shown that α has a significant effect on the average prompt γ-ray multiplicity and energy spectrum [43], as well as the isomer production ratios [48]. In short, increasing the J of the fragments means more γ-ray emission at the expense of neutron emission. These additional γ rays are usually dipole transitions in the continuum region and low in energy. Thus, an increase in α increases $\overline{M}_\gamma$ and softens the overall γ-ray spectrum. The additional γ rays in the continuum lead to a slightly lower prompt neutron multiplicity as well. For this work, we assume equal probability for positive and negative parity in the level density representation of the continuum in the fission fragments, i.e., $P(\pi) = 1/2$.

III. CALCULATIONS

In the past, the de-excitation calculations have sampled from experimental measurements of the mass yields $Y(A)$, or simple parametrizations [20,51]. In this work, we explore the effect on the fission observables from using the

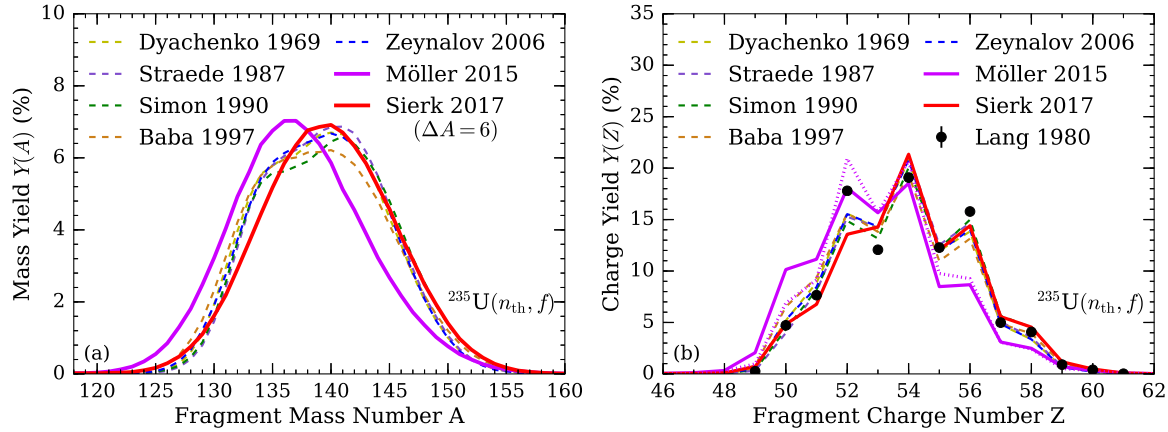

FIG. 2. (a) The pre-neutron-emission mass yields $Y(A)$ for ^{235}U(n_{th}, f) from the various data sources in the three-Gaussian parametrization. The colors correspond to the data source. The thick magenta (red) line is the result of the theoretical calculation by Möller (Sierk) with a $\Delta A = 6.0$ u mass resolution. (b) The charge yields $Y(Z)$ from the various input $Y(A)$ folded with Wahl's [49] $Y(Z|A)$. The dotted line uses the $Y(Z|A)$ of Möller [9]. Black points are the data of Lang *et al.* [50].

calculated yields described in Sec. II A from Refs. [9,11]. Our procedure is straightforward: we conduct the Hauser-Feshbach decay calculations using CGMF with different input $Y(A)$ for ^{235}U(n_{th}, f) and ^{239}Pu(n_{th}, f), both of which have a variety of experimental data available for $Y(A)$ and the various fission observables and correlations. We perform the calculations with the experimental $Y_e(A)$ and with the calculated $Y_c(A)$ to determine if there are noticeable effects on the observables. This sensitivity study is a first step towards determining the predictive capabilities of the calculated fission yields and developing a fully theoretical and consistent fission model. For this work, we only study the impact of using the calculated mass yields, and leave the prospect of using a two-dimensional $Y(A,Z)$ from Ref. [9] or a $Y(A,\mathrm{TKE})$ from Ref. [11] for a future study.

For ^{235}U(n_{th}, f), we take experimental mass yields $Y_e(A)$ from various data sources [33,52–55] and the two calculated mass yields $Y_c(A)$ from Möller [9] and Sierk [11]. For ^{239}Pu(n_{th}, f), we take $Y_e(A)$ from Refs. [24,34,56,57] and the $Y_c(A)$ from Möller [9] and Sierk [11]. We use multiple $Y_e(A)$ in order to determine an uncertainty on the predicted prompt fission observables simply due to the different input experimental mass yields, which is then compared to the values obtained with $Y_c(A)$. Inputs beyond $Y(A)$ are needed to conduct a CGMF calculation. The calculations require a distribution of fragment charge for a given mass $Y(Z|A)$, which is taken from the Wahl systematics [49]. One also needs the average TKE as a function of the fragment mass $\langle\mathrm{TKE}\rangle(A)$, which we take from Ref. [52] and Ref. [56] for ^{235}U(n_{th}, f) and ^{239}Pu(n_{th}, f), respectively. The $R_T(A)$ are deduced in order to best fit $\bar{\nu}(A)$ from Ref. [58] for ^{235}U(n_{th}, f) and from Ref. [59] for ^{239}Pu(n_{th}, f). The α values are chosen to obtain a reasonable agreement with the γ-ray multiplicity distributions of Ref. [60] and the average γ-ray multiplicity $\overline{M}_\gamma$ of Refs. [60–62]. The total summed TKE is allowed to scale by a factor η,

$$\langle\mathrm{TKE}\rangle = \eta \sum_A \langle\mathrm{TKE}\rangle(A) \times Y(A), \tag{7}$$

where the sum is over the heavy fragment masses. In our analyses, η will be given some value to scale the calculated $\bar{\nu}$. Typical values for η are within 0.5% of unity. While experimental $\langle\mathrm{TKE}\rangle$ uncertainties are typically reported as less than 200 keV, these uncertainties are only statistical and the systematic uncertainties can be closer to 0.6%, or 0.5–1.0 MeV [34,63,64]. Thus, while the shape of the $\langle\mathrm{TKE}\rangle(A)$ distribution is relatively well constrained, one can scale the absolute value more freely. The TKE for a particular fission event is sampled from a Gaussian with mean $\langle\mathrm{TKE}\rangle(A)$ and variance $\sigma^2_{\mathrm{TKE}}(A)$, which is taken from Ref. [65] for ^{235}U(n_{th}, f). For ^{239}Pu(n_{th}, f), we use the shape in Ref. [24] for ^{240}Pu(sf). All CGMF calculations in this study contain a total of 640 000 fission events.

Pre-neutron-emission fragment mass and charge yields are presented in Fig. 2 for ^{235}U(n_{th}, f) and in Fig. 3 for ^{239}Pu(n_{th}, f). The dashed lines are the three-Gaussian parametrizations for the different $Y_e(A)$. The thick solid lines are the three-Gaussian parametrizations for the two $Y_c(A)$. We note that the calculated yields $Y_c(A)$ [9,11] have been folded with a mass resolution of $\Delta A \sim 6$ u at FWHM. The resulting charge yields $Y(Z)$ are also given for each reaction. Recall that the $Y(Z|A)$ are from Wahl [49], but the differences in the $Y(A)$ are propagated to the resulting $Y(Z)$, where we see that the changes in the $Y(Z)$ are directly correlated to that in $Y(A)$. For example, the increase between $125 \leqslant A \leqslant 135$ for ^{235}U(n_{th}, f) in the $Y_c(A)$ of Ref. [9] is accompanied by an increase in the charge yields around $49 \leqslant Z \leqslant 51$. The same trends are found in Fig. 3 for ^{239}Pu(n_{th}, f).

An important feature of the fragment mass yields is the average heavy fragment mass $\langle A_h\rangle$. From Eq. (7), one can see that masses with the largest yields, i.e. those near $\langle A_h\rangle$, will dominate the sum and determine the $\langle\mathrm{TKE}\rangle$ to first order. The input $\langle\mathrm{TKE}\rangle(A)$ of Ref. [52] and Ref. [56] both peak near $A = 132$. Thus, mass yields with larger $Y(A \sim 132)$ will result in larger $\langle\mathrm{TKE}\rangle$. From Eq. (3), we note that a larger $\langle\mathrm{TKE}\rangle$ results in a lower $\langle\mathrm{TXE}\rangle$, which provides less energy for the prompt neutron and γ-ray emissions. In addition, a different set of mass yields will generate a change in the Q value for the fission reaction as the fragment masses are different.

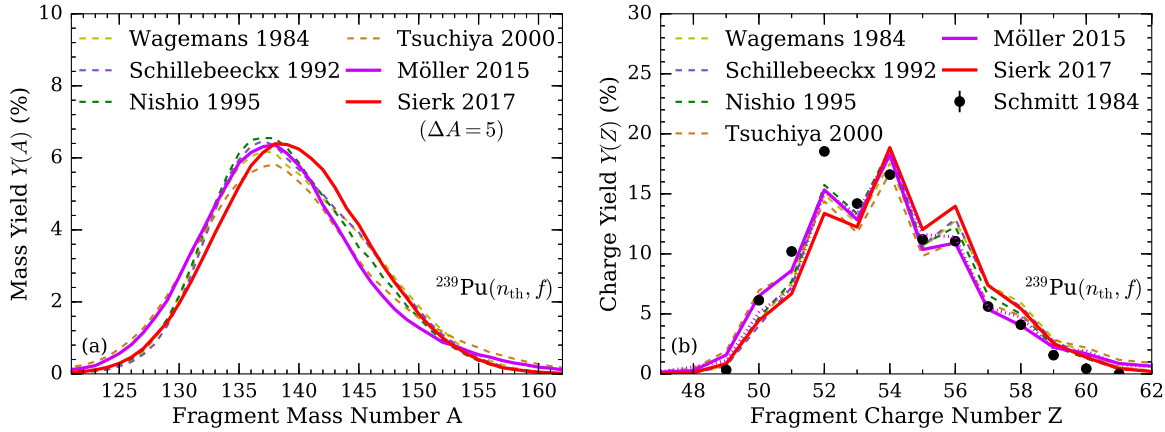

FIG. 3. (a) The pre-neutron-emission mass yields $Y(A)$ for ^{239}Pu$(n_{\rm th}, f)$ from the various data sources in the three-Gaussian parametrization. The colors correspond to the data source. The thick magenta (red) line is the result of the theoretical calculation by Möller (Sierk) with a $\Delta A = 5.0$ u mass resolution. (b) The charge yields $Y(Z)$ from the various input $Y(A)$ folded with Wahl's [49] $Y(Z|A)$. The dotted line uses the $Y(Z|A)$ of Möller [9]. Black points are the data of Schmitt *et al.* [66] using the $Y(A)$ of Ref. [24] as the normalization of the fractional independent yields.

For our calculations, we have either fixed the ⟨TKE⟩ to be 171.40 MeV [25] for ^{235}U$(n_{\rm th}, f)$ and 177.93 MeV [24] for ^{239}Pu$(n_{\rm th}, f)$, or allowed the ⟨TKE⟩ value to float but restrict $\bar{\nu}$ to be in agreement with the IAEA standards [68]: $2.419\,n/f$ for ^{235}U$(n_{\rm th}, f)$ and $2.877\,n/f$ for ^{239}Pu$(n_{\rm th}, f)$.

As seen in Table I, the changes in the mass yields can translate to a change in prompt fission observables. For these CGMF calculations, we used a fixed ⟨TKE⟩, which means that the η values are different for each choice of $Y(A)$ via Eq. (7). This change in η shifts the ⟨TKE⟩(A), which shifts the ⟨TXE⟩(A) in the opposite direction. Thus, lower η values will increase ⟨TXE⟩(A) and result in a larger $\bar{\nu}$ for the fission reaction, as the excitation energy is largely removed by neutron emission [71]. Assuming 5 MeV/n from averaging over all fragments, the statistical differences in the ⟨TKE⟩ values for the calculations in Table I could only account for a difference of 0.4% in $\bar{\nu}$. However, we find that the different $Y(A)$ can produce up to a 7.7% change in $\bar{\nu}$ and a 1.2% change in $\overline{M}_\gamma$. This change in $\overline{M}_\gamma$ is relatively small, compared with the experimental uncertainties [60–62] and could be solely caused by the correlation between $\bar{\nu}$ and $\overline{M}_\gamma$ [72]; i.e., the change in $\overline{M}_\gamma$ is only indirectly related to the change in $Y(A)$ through the change in $\bar{\nu}$. The differences in $\bar{\nu}$, however, are 1–8%, about an order of magnitude larger than the experimental uncertainties [69,70]. This indicates that $\bar{\nu}$ can be very sensitive to the choice of $Y(A)$. The overall trend in Table I is that a $Y(A)$

TABLE I. Average quantities for CGMF calculations utilizing different mass yields for ^{235}U$(n_{\rm th}, f)$ and ^{239}Pu$(n_{\rm th}, f)$. These calculations used ⟨TKE⟩ = 171.40 MeV for ^{235}U$(n_{\rm th}, f)$ [25] and ⟨TKE⟩ = 177.93 MeV for ^{239}Pu$(n_{\rm th}, f)$ [24]. Listed are the average heavy-fragment mass $\langle A_h \rangle$, the heavy-fragment peak variance $\sigma^2_{A_h}$, the average prompt neutron multiplicity $\bar{\nu}$, its first $\langle \nu(\nu-1) \rangle$ and second $\langle \nu(\nu-1)(\nu-2) \rangle$ factorial moments, the average prompt neutron energy in the laboratory frame $\bar{\epsilon}_n^{\rm LAB}$, the average prompt γ-ray multiplicity $\overline{M}_\gamma$, and average γ-ray energy $\bar{\epsilon}_\gamma$. The calculations used an energy threshold of $\epsilon_n^{\rm LAB} > 10$ keV and $\epsilon_\gamma > 100$ keV, as well as a timing window of $\Delta t = 10$ ns for the γ rays. Values from ENDF/B-VIII.0 [67] are also listed with similar detection thresholds.

	Input $Y(A)$	$\langle A_h \rangle$ (u)	$\sigma^2_{A_h}$ (u^2)	$\bar{\nu}$ (n/f)	$\langle \nu(\nu-1) \rangle$	$\langle \nu(\nu-1)(\nu-2) \rangle$	$\bar{\epsilon}_n^{\rm LAB}$ (MeV)	$\overline{M}_\gamma$ (γ/f)	$\bar{\epsilon}_\gamma$ (MeV)
^{235}U$(n_{\rm th}, f)$	Dyachenko [52]	139.16	28.69	2.458	4.766	6.749	1.984	7.284	0.856
	Straede [53]	139.50	27.27	2.423	4.620	6.390	1.974	7.308	0.851
	Simon [54]	139.74	30.59	2.382	4.457	6.020	1.967	7.311	0.852
	Baba [55]	139.00	32.88	2.458	4.772	6.783	1.988	7.274	0.860
	Zeynalov [33]	139.17	28.63	2.454	4.751	6.710	1.983	7.294	0.855
	Möller [9]	137.39	33.57	2.621	5.485	8.618	2.029	7.189	0.876
	Sierk [11]	139.73	31.47	2.373	4.438	6.034	1.963	7.313	0.850
ENDF/B-VIII.0 [67]				2.414 ± 0.01	4.641	6.716	2.00 ± 0.01	8.19	0.89
^{239}Pu$(n_{\rm th}, f)$	Wagemans [56]	139.67	41.86	2.887	6.766	12.13	1.998	7.711	0.864
	Schillebeeckx [24]	139.61	39.65	2.901	6.828	12.31	2.001	7.715	0.863
	Nishio [34]	139.13	38.77	2.948	7.058	12.97	2.017	7.695	0.867
	Tsuchiya [57]	139.21	57.48	2.875	6.711	12.00	2.001	7.668	0.877
	Möller [9]	138.82	48.53	2.955	7.097	13.11	2.019	7.658	0.876
	Sierk [11]	139.68	38.90	2.888	6.777	12.18	1.994	7.742	0.860
ENDF/B-VIII.0 [67]				2.870 ± 0.01	6.721	12.51	2.117 ± 0.037	7.33	0.87

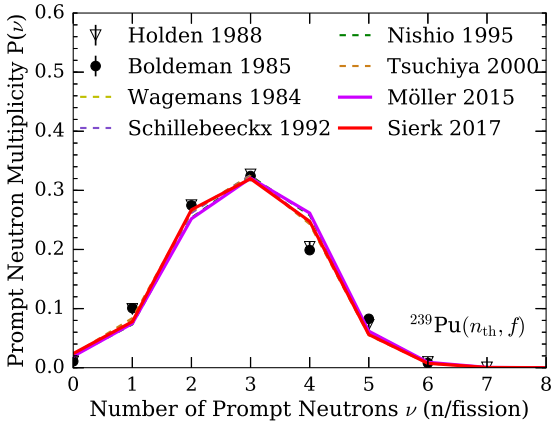

FIG. 4. The prompt neutron multiplicity distribution $P(\nu)$ of ^{239}Pu$(n_{\rm th}, f)$ for the various input experimental $Y_e(A)$ (dashed lines) or calculated $Y_c(A)$ (thick solid lines). Black points are the data of Boldeman [69] and Holden [70].

with $\langle A_h \rangle$ closer to 132 will result in a lower η to maintain a fixed $\langle$TKE$\rangle$. This will then increase $\langle$TXE$\rangle$ and produce more prompt neutrons. Figure 4 demonstrates this point for ^{239}Pu$(n_{\rm th}, f)$. We note that the factorial moments of $P(\nu)$ are very sensitive to the variance $\sigma^2_{\rm TKE}(A)$. A scaling of $\sigma^2_{\rm TKE}(A)$ by 0.76 for ^{235}U$(n_{\rm th}, f)$ and 0.81 for ^{239}Pu$(n_{\rm th}, f)$ was used to obtain reasonable agreement with the experimental $P(\nu)$ [69,70]. All calculations shown in this work use the same $\sigma^2_{\rm TKE}(A)$ and the same scaling, meaning that the changes in $P(\nu)$ seen in Fig. 4 are a direct result of the change in $Y(A)$ only.

From our initial calculations, we can already see that differences in $Y(A)$ can produce changes in $\bar{\nu}$ above the sub-percent reported uncertainties for both ^{235}U$(n_{\rm th}, f)$ and ^{239}Pu$(n_{\rm th}, f)$ evaluated by the standards group [68]. We can invert the procedure to instead fix $\bar{\nu}$ to the evaluated values and determine the corresponding $\langle$TKE$\rangle$ value needed. This procedure, and its comparison with the method of fixing $\langle$TKE$\rangle$, is shown in Fig. 5. The different $Y(A)$ induce typical errors of $\delta\langle$TKE$\rangle \sim 0.4\%$ and $\delta\bar{\nu} \sim 4\%$. One intriguing result from this study is that a highly precise measurement of $\bar{\nu}$ could be used to constrain the allowed values for $\langle$TKE$\rangle$, as already mentioned in Ref. [73]. In the bottom plot of Fig. 5, when we fix $\bar{\nu}$ to the evaluated value, the spread in $\langle$TKE$\rangle$ values induced from the choice of $Y(A)$ is within the $\pm$0.5 MeV range. This implies that the experimental uncertainty on $\langle$TKE$\rangle$, 1.4 MeV in Ref. [25], could be reduced by the constraints on $\bar{\nu}$ by about a factor of 3. The differences in the input mass yields seem to limit this type of correlation analysis to about $\pm$0.4 MeV in the $\langle$TKE$\rangle$ uncertainties. We note that the average spin of the fragments, governed by α, and the shape of $\langle$TKE$\rangle(A)$ will also influence the correlation between $\langle$TKE$\rangle$ and $\bar{\nu}$.

The changes in the prompt fission neutron spectrum (PFNS) and prompt fission γ-ray spectrum (PFGS) are shown in Figs. 6 and 7. The PFNS is plotted to illustrate the impact of the different $Y(A)$ at low outgoing neutron energies. We can see that mass yields shifted closer to symmetry will have a slightly harder PFNS, as the average neutron energies are larger for these masses [25,57,76]. Even with this shift, the typical error

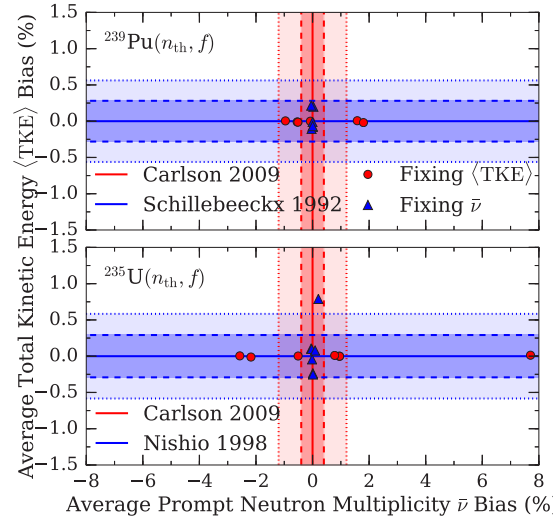

FIG. 5. The correlation between the average total kinetic energy of the fragments $\langle$TKE$\rangle$ and the average prompt neutron multiplicity $\bar{\nu}$ for ^{235}U$(n_{\rm th}, f)$ (bottom) and ^{239}Pu$(n_{\rm th}, f)$ (top). The calculations have either a fixed $\langle$TKE$\rangle$ (circles) or a fixed $\bar{\nu}$ (triangles). Horizontal lines are the experimental $\langle$TKE$\rangle$ for ^{235}U$(n_{\rm th}, f)$ [25] and ^{239}Pu$(n_{\rm th}, f)$ [24] with the shaded regions representing $\pm$0.5 MeV (dashed darker region) and $\pm$1.0 MeV (dotted lighter region). Vertical lines are the evaluated $\bar{\nu}$ and their 1σ (dashed darker region) and 3σ (dotted lighter region) uncertainty bands [68].

on the average outgoing neutron energy from using calculated mass yields is $\delta\bar{\epsilon}_n^{\rm LAB} \sim 1\%$. Overall, the PFNS is mostly insensitive to the choice of input $Y(A)$. An additional note is that the PFNS calculated by CGMF are consistently softer than the experimental ones for neutron energies above 4 MeV, an issue also identified in previous studies [20,47]. This work demonstrates that the choice of input mass yields does not seem to account for this discrepancy.

The PFGS in Fig. 7 also appears relatively insensitive to the choice of input $Y(A)$. We note that the calculation of

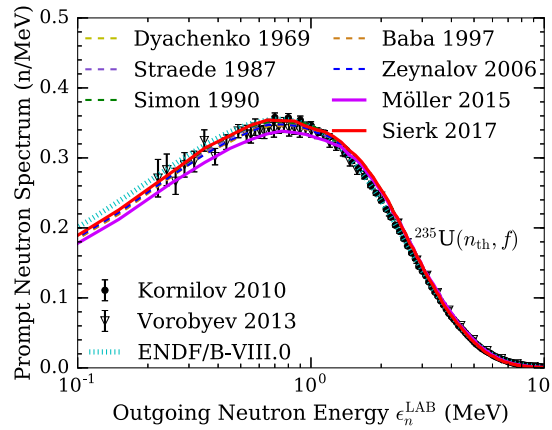

FIG. 6. The normalized prompt fission neutron spectrum (PFNS) of ^{235}U$(n_{\rm th}, f)$ in the laboratory frame calculated with the various input experimental $Y_e(A)$ (dashed lines) or calculated $Y_c(A)$ (thick solid lines). Black points are the data of Kornilov *et al.* [74] and Vorobyev *et al.* [75]. The dotted line is from ENDF/B-VIII.0 [67].

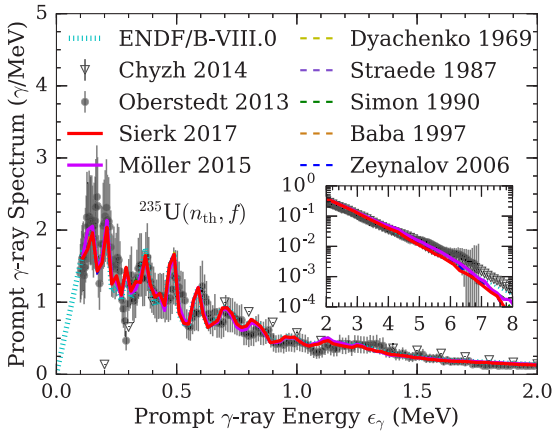

FIG. 7. The normalized prompt fission γ-ray spectrum (PFGS) of ^{235}U(n_{th}, f) calculated with the various input experimental $Y_e(A)$ (dashed lines) or calculated $Y_c(A)$ (thick solid lines). Black points are the data of Oberstedt *et al.* [61] and Chyzh *et al.* [60]. A 100 keV energy threshold and a 10 ns timing window were used, as in Ref. [61]. The dotted line is from ENDF/B-VIII.0 [67]. The inset shows the high-energy region.

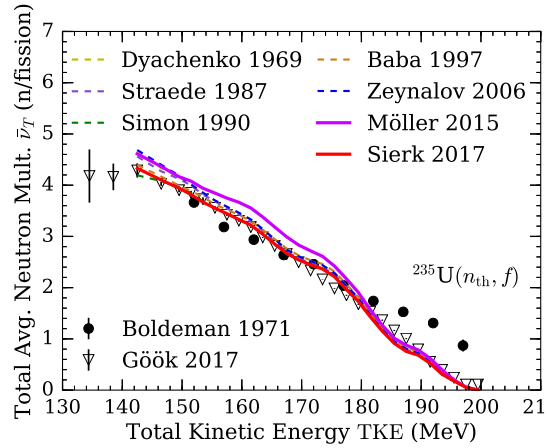

FIG. 8. The correlation between the total kinetic energy of the fission fragments and the average total prompt neutron multiplicity between both the light and heavy fission fragments, $\bar{\nu}_T$(TKE), of ^{235}U(n_{th}, f) for various input experimental $Y_e(A)$ (dashed lines) or calculated $Y_c(A)$ (thick solid lines). Black points are the data from Boldeman *et al.* [81] and Göök *et al.* [80].

^{235}U(n_{th}, f) using the $Y(A)$ from Möller [9] produces a slightly harder PFGS as the mass yields are more shifted towards the $N = 82$ closed shell, where the average γ-ray energy is known to peak [77,78] due to the large level spacing. A similar argument reveals why the average γ-ray energy for the Tsuchiya *et al.* [57] mass yields is relatively large. Even though its average heavy fragment peak is not the closest to $A = 132$, the peak width is large enough to produce larger yields for $A \sim 132$ than the other input yields, as seen in Fig. 3(a). Thus, *both* $\langle A_h \rangle$ *and* $\sigma^2_{A_h}$ can impact the prompt fission observables. We note that specific γ-ray lines are sensitive to the choice of input mass yields, as seen in Fig. 7. For example, the 212.53 keV peak of ^{100}Zr is 5% more intense with the $Y_c(A)$ of Möller [9] instead of Sierk [11], due to the change in peak location seen in Fig. 2(a). Overall, typical errors of $\delta\bar{\epsilon}_\gamma \sim 1\%$ occur when using the calculated yields over experimental ones. We note that recent studies involving significantly different mass yields, such as those between spontaneous fission and neutron-induced fission from the same compound nucleus, can generate a measurable difference in the PFGS [79]. In Fig. 7, the calculated spectra deviate from the experimental data above $\epsilon_\gamma = 5$ MeV, with the CGMF calculations underpredicting the measured spectrum. Previous studies [43,48] have demonstrated that decreasing the spin-scaling factor α can increase the slope of the PFGS, but this will lower $\overline{M}_\gamma$, creating tension with the values of Refs. [60–62].

We now turn to the correlation between the total kinetic energy and the total number of prompt neutrons emitted from both the light and heavy fragment $\bar{\nu}_T$. This relation utilizes the energy conservation in Eq. (3) and is expected to be anticorrelated, as a larger TKE results in less energy available for prompt neutron emission. In Fig. 8, this is seen by the decreasing trend of $\bar{\nu}_T$(TKE) for ^{235}U(n_{th}, f). The CGMF calculations reproduce the experimental data of Göök *et al.* [80] very well. A possible explanation for the differences seen for TKE > 180 MeV is a broader TKE resolution in Boldeman *et al.* [81]. The TKE bins below 140 MeV have poor statistics in the CGMF calculations, so we have cut the calculated curves at this value. We note two trends seen in Fig. 8. First, mass yields with a lower $\langle A_h \rangle$ require a lower η to keep $\langle$TKE$\rangle$ fixed, which results in more excitation energy available for the fragments and a shift towards higher $\bar{\nu}_T$(TKE). Second, mass yields with wider peaks (larger $\sigma^2_{A_h}$) result in a shallower slope for the TKE < 160 MeV bins. For example, the result using $Y_e(A)$ from Baba *et al.* [55] is very similar to the result when using $Y_e(A)$ from Refs. [33,52,53] for TKE > 160 MeV, but becomes closer to the result using $Y_c(A)$ from Sierk [11] for TKE < 160 MeV. When we take a single $Y(A)$ and arbitrarily add a mass resolution, which keeps $\langle A_h \rangle$ about constant while increasing $\sigma^2_{A_h}$, we find the same trend. This occurs because a larger $\sigma^2_{A_h}$ introduces a wider variety of mass yields contributing to the same TKE energy bin. In particular, for the lower TKE energy bins, the contribution of very asymmetric yields increases, which also tend to have a low $\bar{\nu}_T$ [58]. This additional influence of very asymmetric mass splits lowers the $\bar{\nu}_T$ for that TKE energy bin, thus resulting in the trend seen in Fig. 8. This low-TKE region is difficult for experiments, where correcting for detector effects, such as neutron scattering, capture efficiency, and the recoil imparted onto the fragment, can play a large role [58,76,82,83]. Overall, we find that the shift towards higher $\bar{\nu}_T$(TKE) is primarily due to the different $\langle A_h \rangle$, while the change in the slope of $\bar{\nu}_T$(TKE) at low TKE values is due to the different $\sigma^2_{A_h}$.

IV. CONCLUSION

We have used theoretical models for the fragment mass yields [9,11] as input for Hauser-Feshbach simulations of the emission of prompt neutrons and γ rays [20]. This allows us to test the feasibility of using theoretically calculated fission-fragment yields and determine the sensitivity of important

TABLE II. Correlation between calculated $\bar{\nu}$ and the input average heavy fragment mass $\langle A_h \rangle$ for ^{235}U$(n_{\rm th}, f)$ and ^{239}Pu$(n_{\rm th}, f)$. Also listed are the biases for several prompt fission observables from using calculated mass yields of Möller [9] and Sierk [11], as well as experimental or evaluated uncertainties for reference.

$\partial\bar{\nu}/\partial\langle A_h\rangle$ $(n/f/\mathrm{u})$	^{235}U$(n_{\rm th}, f)$ ± 0.11			^{239}Pu$(n_{\rm th}, f)$ ± 0.08		
	Möller [9]	Sierk [11]	Exp. or Eval.	Möller [9]	Sierk [11]	Exp. or Eval.
$\delta\langle$TKE$\rangle$ (MeV)	0.8%	0.3%	0.6% [64]	0.2%	0.1%	0.6% [64]
$\delta\bar{\nu}$ (n/f)	7.7%	2.6%	0.4% [84]	1.8%	0.5%	0.3% [84]
$\delta\bar{\epsilon}_n^{\rm LAB}$ (MeV)	2.5%	0.8%	0.5% [75]	0.7%	0.5%	1.7% [85]
$\delta\overline{M}_\gamma$ (γ/f)	1.2%	0.5%	1.3% [61]	0.3%	0.3%	1.6% [62]
$\delta\bar{\epsilon}_\gamma$ (MeV)	2.1%	0.9%	2.4% [61]	0.8%	0.7%	2.4% [62]

prompt fission observables, such as the average prompt neutron multiplicity $\bar{\nu}$, average total kinetic energy of the fragments $\langle$TKE$\rangle$, and average energies of the emitted neutrons and γ rays, to the input yields. We utilize the ^{235}U$(n_{\rm th}, f)$ and ^{239}Pu$(n_{\rm th}, f)$ reactions, as there is significant experimental data for both the mass yields $Y(A)$ and prompt fission observables. An initial comparison of the mass yields demonstrates that the calculated yields can achieve reasonable agreement with most experimental data. Using a Monte Carlo implementation of the Hauser-Feshbach statistical decay model [45], we propagate the differences between the experimental and calculated mass yields to differences in the prompt neutron and γ-ray observables. In particular, we find that the average heavy fragment mass $\langle A_h \rangle$ is very influential in determining $\langle$TKE$\rangle$, which, in turn, is a major factor in determining $\bar{\nu}$. This finding is reflected in Table II, where we list the correlation between the calculated $\bar{\nu}$ and input $\langle A_h \rangle$. The correlation is determined by fitting ordered pairs of $(\langle A_h \rangle, \bar{\nu})$ for each set of mass yields in Table I. This correlation implies that, when all other input is kept constant, two mass yields with heavy fragment peaks one mass unit apart will result in a $\bar{\nu}$ differing by about $0.1\,n/f$. Very different peak widths $\sigma^2_{A_h}$ complicate the correlation. We note that this analysis relies on the shape of the $\langle$TKE$\rangle(A)$ we have chosen, but not on the overall $\langle$TKE$\rangle$, which only shift the ordered pairs and leave the correlation unaffected.

Also listed in Table II are the biases on the various prompt fission observables from the use of calculated yields instead of experimental ones. We find that both the location of the mass peak $\langle A_h \rangle$ and the width of the peak $\sigma^2_{A_h}$, where wider peaks resulting in an increased yield near the $N = 82$ shell closure, could result in a slightly harder PFNS and PFGS. Specific discrete γ-ray intensities are also directly affected by the choice of mass yields. The width of the mass peak was also found to impact the correlation between the total kinetic energy of the fragments and the average total prompt neutron multiplicity.

These correlations and derived biases will help inform future fission-yield models and the de-excitation procedure. These calculations can be improved with self-consistent $Y(A,Z)$ yields from Ref. [9] and $Y(A,$TKE$)$ yields from Ref. [11]. In a future study, we plan to implement the exact fission-fragment mass yields into the Hauser-Feshbach statistical-decay model and apply the effects of the experimental mass and energy resolutions to the calculated results, instead of applying a mass resolution to the input mass yields. Additional experimental data of the fragment mass, charge, and kinetic energies at a variety of incident neutron energies, such as in Refs. [86,87], would allow for a more critical comparison of the calculated and experimental yields. Furthermore, measurements of the fragment yields for exotic nuclei will improve our ability to benchmark calculated yields outside the more well-studied actinide chains. When calculating the prompt neutron and γ-ray emissions, several input parameters are needed, but may not possess the proper energy dependence as there are no data available. For example, the dependence of $\langle$TKE$\rangle(A)$ on incident neutron energy has only been determined for a limited number of nuclei [86,87]. In addition, properties of the prompt γ rays have seldom been measured at higher incident neutron energies [88], but additional data may provide useful information about the spins of fission fragments at these energies. Finally, measurements conducted by Naqvi *et al.* [89] demonstrated that $\bar{\nu}(A)$ has a distinct change in shape for higher incident neutron energies, but further experimental tests of this would provide useful insight into the excitation energy sharing in fission.

Our results utilize theoretical methods to calculate fission observables from scission to prompt neutron and γ-ray emissions, a step towards a predictive model of fission. In general, we find that the use of calculated yields do not yet possess the precision needed for very sensitive criticality estimates [90] or neutron correlation counting [91]. However, it should be noted that the variance on $\bar{\nu}$ induced simply from the differences in the experimental mass yields is already near the uncertainties of the IAEA standards [68]. For applications that do not require this degree of accuracy, we find that the use of calculated mass yields and the prompt particle emission through a Hauser-Feshbach treatment is invaluable, especially where there are little to no experimental data, as is the case in many nuclides participating in the *r* process [23]. Furthermore, the prompt γ-ray observables appear less sensitive to the use of calculated mass yields instead of experimental ones, suggesting that estimates of γ-ray heating for reactor design could be done for nuclides without experimental data using a combination of theoretical mass yields and a Hauser-Feshbach decay treatment, as we have used here, and still satisfy the needed design uncertainties [92].

ACKNOWLEDGMENTS

The authors would like to thank A. Göök for providing recent data and T. Kawano, I. Stetcu, and M. White for helpful conversations and support. This work was supported by the Office of Defense Nuclear Nonproliferation Research & Development (DNN R&D), National Nuclear Security Administration, US Department of Energy. It was performed under the auspices of the National Nuclear Security Administration of the US Department of Energy at Los Alamos National Laboratory under Contract No. DEAC52-06NA25396.

[1] O. Hahn and F. Straßmann, Naturwissenschaften **27**, 11 (1939).
[2] L. Meitner and O. Frisch, Nature (London) **143**, 239 (1939).
[3] N. Bohr, Nature (London) **143**, 330 (1939).
[4] N. Bohr and J. A. Wheeler, Phys. Rev. **56**, 426 (1939).
[5] P. Möller, A. J. Sierk, T. Ichikawa, A. Iwamoto, R. Bengtsson, H. Uhrenholt, and S. Åberg, Phys. Rev. C **79**, 064304 (2009).
[6] J. Randrup and P. Möller, Phys. Rev. C **88**, 064606 (2013).
[7] N. Bohr, Nature (London) **137**, 344 (1936).
[8] J. Randrup and P. Möller, Phys. Rev. Lett. **106**, 132503 (2011).
[9] P. Möller and T. Ichikawa, Eur. Phys. J. A **51**, 173 (2015).
[10] Y. Aritomo, S. Chiba, and F. Ivanyuk, Phys. Rev. C **90**, 054609 (2014).
[11] A. J. Sierk, Phys. Rev. C **96**, 034603 (2017).
[12] N. Schunck, D. Duke, H. Carr, and A. Knoll, Phys. Rev. C **90**, 054305 (2014).
[13] D. Regnier, N. Dubray, N. Schunck, and M. Verrière, Phys. Rev. C **93**, 054611 (2016).
[14] P. Goddard, P. Stevenson, and A. Rios, Phys. Rev. C **92**, 054610 (2015).
[15] A. Bulgac, P. Magierski, K. J. Roche, and I. Stetcu, Phys. Rev. Lett. **116**, 122504 (2016).
[16] P. Talou, T. Kawano, and I. Stetcu, Phys. Proc. **47**, 39 (2013).
[17] R. Vogt and J. Randrup, Nucl. Data Sheets **118**, 220 (2014).
[18] O. Litaize, O. Serot, and L. Berge, Eur. Phys. J. A **51**, 177 (2015).
[19] M. R. Mumpower, T. Kawano, and P. Möller, Phys. Rev. C **94**, 064317 (2016).
[20] B. Becker, P. Talou, T. Kawano, Y. Danon, and I. Stetcu, Phys. Rev. C **87**, 014617 (2013).
[21] K.-H. Schmidt, S. Steinhäuser, C. Böckstiegel, A. Grewe, A. Heinz, A. Junghans, J. Benlliure, H.-G. Clerc, M. de Jong, J. Müller *et al.*, Nucl. Phys. A **665**, 221 (2000).
[22] K. Nishio, K. Hirose, R. Léguillon, H. Makii, R. Orlandi, K. Tsukada, J. Smallcombe, S. Chiba, Y. Aritomo, S. Tanaka *et al.*, EPJ Web Conf. **146**, 04009 (2017).
[23] B. Côté, C. Fryer, K. Belczynski, O. Korobkin, M. Chruślińska, N. Vassh, M. Mumpower, J. Lippuner, T. Sprouse, R. Surman *et al.*, arXiv:1710.05875.
[24] P. Schillebeeckx, C. Wagemans, A. Deruytter, and R. Barthélémy, Nucl. Phys. A **545**, 623 (1992).
[25] K. Nishio, Y. Nakagome, H. Yamamoto, and I. Kimura, Nucl. Phys. A **632**, 540 (1998).
[26] P. Schillebeeckx, C. Wagemans, P. Geltenbort, F. Gönnenwein, and A. Oed, Nucl. Phys. A **580**, 15 (1994).
[27] J.-F. Martin, J. Taieb, A. Chatillon, G. Bélier, G. Boutoux, A. Ebran, T. Gorbinet, L. Grente, B. Laurent, E. Pellereau *et al.*, Eur. Phys. J. A **51**, 174 (2015).
[28] Y. K. Gupta, D. C. Biswas, O. Serot, D. Bernard, O. Litaize, S. Julien-Laferrière, A. Chebboubi, G. Kessedjian, C. Sage, A. Blanc *et al.*, Phys. Rev. C **96**, 014608 (2017).
[29] F. Tovesson, D. Mayorov, D. Duke, B. Manning, and V. Geppert-Kleinrath, EPJ Web Conf. **146**, 04010 (2017).
[30] J. Randrup, P. Möller, and A. J. Sierk, Phys. Rev. C **84**, 034613 (2011).
[31] P. Möller and C. Schmitt, Eur. Phys. J. A **53**, 7 (2017).
[32] U. Brosa, S. Grossmann, and A. Müller, Phys. Rep. **197**, 167 (1990).
[33] S. Zeynalov, V. Furman, F.-J. Hambsch, M. Florec, V. Konovalov, V. Khryachkov, and Y. Zamyatnin, in *Proceedings of the XIII International Seminar on Interaction of Neutrons with Nuclei* (JINR, Dubna, 2006), pp. 351–359.
[34] K. Nishio, Y. Nakagome, I. Kanno, and I. Kimura, J. Nucl. Sci. Technol. **32**, 404 (1995).
[35] W. Hauser and H. Feshbach, Phys. Rev. **87**, 366 (1952).
[36] A. Koning and J. Delaroche, Nucl. Phys. A **713**, 231 (2003).
[37] J. Kopecky and M. Uhl, Phys. Rev. C **41**, 1941 (1990).
[38] R. Capote, M. Herman, P. Obložinský, P. Young, S. Goriely, T. Belgya, A. Ignatyuk, A. Koning, S. Hilaire, V. Plujko *et al.*, Nucl. Data Sheets **110**, 3107 (2009), Special Issue on Nuclear Reaction Data.
[39] A. Gilbert and A. G. W. Cameron, Can. J. Phys. **43**, 1446 (1965).
[40] O. Litaize and O. Serot, Phys. Rev. C **82**, 054616 (2010).
[41] K.-H. Schmidt and B. Jurado, Phys. Rev. Lett. **104**, 212501 (2010).
[42] K.-H. Schmidt and B. Jurado, Phys. Rev. C **83**, 061601 (2011).
[43] I. Stetcu, P. Talou, T. Kawano, and M. Jandel, Phys. Rev. C **90**, 024617 (2014).
[44] A. Tudora, F.-J. Hambsch, I. Visan, and G. Giubega, Nucl. Phys. A **940**, 242 (2015).
[45] P. Talou, T. Kawano, and I. Stetcu, Los Alamos National Laboratory Report No. LA-CC-13063,2013 (unpublished).
[46] T. Kawano, P. Talou, M. B. Chadwick, and T. Watanabe, J. Nucl. Sci. Technol. **47**, 462 (2010).
[47] T. Kawano, P. Talou, I. Stetcu, and M. Chadwick, Nucl. Phys. A **913**, 51 (2013).
[48] I. Stetcu, P. Talou, T. Kawano, and M. Jandel, Phys. Rev. C **88**, 044603 (2013).
[49] A. C. Wahl, Los Alamos National Laboratory Report No. LA-13928, 2002 (unpublished).
[50] W. Lang, H.-G. Clerc, H. Wohlfarth, H. Schrader, and K.-H. Schmidt, Nucl. Phys. A **345**, 34 (1980).
[51] R. Vogt, J. Randrup, J. Pruet, and W. Younes, Phys. Rev. C **80**, 044611 (2009).
[52] P. Dyachenko, B. Kuzminov, and M. Tarasko, Sov. J. Nucl. Phys. **8**, 165 (1969).
[53] C. Straede, C. Budtz-Jørgensen, and H.-H. Knitter, Nucl. Phys. A **462**, 85 (1987).
[54] G. Simon, J. Trochon, F. Brisard, and C. Signarbieux, Nucl. Instrum. Methods Phys. Res., Sect. A **286**, 220 (1990).
[55] H. Baba, T. Saito, N. Takahashi, A. Yokoyama, T. Miyauchi, S. Mori, D. Yano, T. Hakoda, K. Takamiya, K. Nakanishi *et al.*, J. Nucl. Sci. Technol. **34**, 871 (1997).
[56] C. Wagemans, E. Allaert, A. Deruytter, R. Barthélémy, and P. Schillebeeckx, Phys. Rev. C **30**, 218 (1984).

[57] C. Tsuchiya, Y. Nakagome, H. Yamana, H. Moriyama, K. Nishio, I. Kanno, K. Shin, and I. Kimura, J. Nucl. Sci. Technol. **37**, 941 (2000).
[58] A. S.Vorobyev, O. A. Shcherbakov, A. M. Gagarski, G. V. Val'ski, and G. A. Petrov, EPJ Web Conf. **8**, 03004 (2010).
[59] V. Apalin, Y. Gritsyuk, I. Kutikov, V. Lebedev, and L. Mikaelian, Nucl. Phys. **71**, 553 (1965).
[60] A. Chyzh, C. Y. Wu, E. Kwan, R. A. Henderson, T. A. Bredeweg, R. C. Haight, A. C. Hayes-Sterbenz, H. Y. Lee, J. M. O'Donnell, and J. L. Ullmann, Phys. Rev. C **90**, 014602 (2014).
[61] A. Oberstedt, T. Belgya, R. Billnert, R. Borcea, T. Bryś, W. Geerts, A. Göök, F.-J. Hambsch, Z. Kis, T. Martinez *et al.*, Phys. Rev. C **87**, 051602 (2013).
[62] A. Gatera, T. Belgya, W. Geerts, A. Göök, F.-J. Hambsch, M. Lebois, B. Maróti, A. Moens, A. Oberstedt, S. Oberstedt *et al.*, Phys. Rev. C **95**, 064609 (2017).
[63] J. Milton and J. Fraser, Can. J. Phys. **40**, 1626 (1962).
[64] C. Wagemans, *The Nuclear Fission Process* (CRC, Boca Raton, FL, 1991).
[65] V. P. Zakharova, D. K. Ryazanov, B. G. Basova, A. D. Rabinovich, and V. A. Korostylev, Yadern. Fiz. **18**, 710 (1973) [Sov. J. Nucl. Phys. **16**, 364 (1973)].
[66] C. Schmitt, A. Guessous, J. Bocquet, H.-G. Clerc, R. Brissot, D. Engelhardt, H. Faust, F. Gönnenwein, M. Mutterer, H. Nifenecker *et al.*, Nucl. Phys. A **430**, 21 (1984).
[67] D. A. Brown *et al.*, Nucl. Data Sheets **148**, 1 (2018).
[68] A. Carlson, V. Pronyaev, D. Smith, N. Larson, Z. Chen, G. Hale, F.-J. Hambsch, E. Gai, S.-Y. Oh, S. Badikov *et al.*, Nucl. Data Sheets **110**, 3215 (2009), Special Issue on Nuclear Reaction Data.
[69] J. W. Boldeman and M. G. Hines, Nucl. Sci. Eng. **91**, 114 (1985).
[70] N. E. Holden and M. S. Zucker, Nucl. Sci. Eng. **98**, 174 (1988).
[71] P. Talou, T. Kawano, I. Stetcu, J. P. Lestone, E. McKigney, and M. B. Chadwick, Phys. Rev. C **94**, 064613 (2016).
[72] T. Wang, G. Li, L. Zhu, Q. Meng, L. Wang, H. Han, W. Zhang, H. Xia, L. Hou, R. Vogt *et al.*, Phys. Rev. C **93**, 014606 (2016).
[73] J. Randrup, P. Talou, and R. Vogt, EPJ Web Conf. **146**, 04003 (2017).
[74] N. Kornilov, F.-J. Hambsch, I. Fabry, S. Oberstedt, T. Belgya, Z. Kis, L. Szentmiklosi, and S. Simakov, Nucl. Sci. Eng. **165**, 117 (2010).
[75] R. Capote, Y.-J. Chen, F.-J. Hambsch, N. Kornilov, J. Lestone, O. Litaize, B. Morillon, D. Neudecker, S. Oberstedt, T. Ohsawa *et al.*, Nucl. Data Sheets **131**, 1 (2016), Special Issue on Nuclear Reaction Data.
[76] A. Göök, F.-J. Hambsch, and M. Vidali, Phys. Rev. C **90**, 064611 (2014).
[77] F. Pleasonton, R. L. Ferguson, and H. W. Schmitt, Phys. Rev. C **6**, 1023 (1972).
[78] A. Hotzel, P. Thirolf, C. Ender, D. Schwalm, M. Mutterer, P. Singer, M. Klemens, J. P. Theobald, M. Hesse, F. Gönnenwein *et al.*, Z. Phys. A **356**, 299 (1987).
[79] A. Chyzh, P. Jaffke, C.-Y. Wu, R. Henderson, P. Talou, I. Stetcu, J. Henderson, B. Q., S. Sheets, R. Hughes *et al.* (unpublished).
[80] A. Göök, F.-J. Hambsch, and S. Oberstedt, EPJ Web Conf. **169**, 00004 (2018).
[81] J. Boldeman, A. de L.Musgrove, and R. Walsh, Aust. J. Phys. **24**, 821 (1971).
[82] A. Gavron, Nucl. Instrum. Methods **115**, 99 (1974).
[83] H. Nifenecker, C. Signarbieux, R. Babinet, and J. Poitou, in *Proceedings of the Third IAEA Symposium on the Physics and Chemistry of Fission* (IAEA, Vienna, 1974), pp 117–178.
[84] M. B. Chadwick *et al.*, Nucl. Data Sheets **148**, 189 (2018).
[85] D. Neudecker, P. Talou *et al.*, Nucl. Data Sheets (to be published).
[86] D. L. Duke, F. Tovesson, A. B. Laptev, S. Mosby, F.-J. Hambsch, T. Bryś, and M. Vidali, Phys. Rev. C **94**, 054604 (2016).
[87] K. Meierbachtol, F. Tovesson, D. L. Duke, V. Geppert-Kleinrath, B. Manning, R. Meharchand, S. Mosby, and D. Shields, Phys. Rev. C **94**, 034611 (2016).
[88] J. Fréhaut, A. Bertin, and R. Bois, in *Nuclear Data for Science and Technology: Proceedings of the International Conference Antwerp, 6–10 September 1982*, edited by K. H. Böckhoff (Springer Netherlands, Dordrecht, 1983), pp. 78–81 (in French).
[89] A. A. Naqvi, F. Käppeler, F. Dickmann, and R. Müller, Phys. Rev. C **34**, 218 (1986).
[90] D. Neudecker, T. Taddeucci, R. Haight, H. Lee, M. White, and M. Rising, Nucl. Data Sheets **131**, 289 (2016), Special Issue on Nuclear Reaction Data.
[91] S. Croft, S. L. Cleveland, and A. D. Nicholson, Oak Ridge National Laboratory (ORNL) Report No. INMM56-2015, 2015 (unpublished).
[92] G. Rimpault, D. Bernard, D. Blanchet, C. Vaglio-Gaudard, S. Ravaux, and A. Santamarina, Phys. Proc. **31**, 3 (2012).